Chemical Science

ROYAL SOCIETY OF CHEMISTRY

EDGE ARTICLE

View Article Online
View Journal

Cite this: DOI: 10.1039/d6sc03014a

All publication charges for this article have been paid for by the Royal Society of Chemistry

Spatial decoupling of CH_4 oxidation and CO_2 reduction enables near-stoichiometric dry reforming of methane

Wenbin Li, Jiyun Ren, Wenjie Guo, Qing Guo, Sai Zhang * and Yongquan Qu *

Received 11th April 2026
Accepted 1st June 2026

DOI: 10.1039/d6sc03014a

rsc.li/chemical-science

The practical application of dry reforming of methane (DRM) is hindered by catalyst deactivation, primarily due to the deviation of the ideal 1 : 1 H_2 : CO stoichiometry for competitive CH_4 and CO_2 adsorption/activation. Excessive CH_4 decomposition results in H_2 : CO > 1 with carbon deposition, while predominant CO_2 chemisorption leads to H_2 : CO < 1 with the favorable reverse water-gas shift (RWGS) side reaction. Herein, we demonstrate an *O-migration coupling strategy on Pt/CeO_2 featuring Pt clusters and frustrated Lewis pairs (FLPs, consisting of two Ce^{3+} and one lattice oxygen) to achieve near-stoichiometric and durable DRM. The FLP sites on the CeO_2 support, independent of Pt–CeO_2 interfaces, reduce CO_2 to CO while generating *O species. These *O species migrate to Pt clusters, driving the partial CH_4 oxidation. Through this *O-migration-enabled spatial decoupling of CO_2 reduction and CH_4 oxidation, the catalyst delivers a near-stoichiometric H_2 : CO ratio of 0.99 and an unprecedented CH_4 conversion rate of 93.9 mol g_{Pt}^{-1} h^{-1} at 700 °C. Moreover, stable performance is exhibited for over 400 h, with a turnover number exceeding 7 200 000. This work establishes oxygen migration coupling as a potential strategy for spatially decoupled redox catalysis beyond DRM.

Introduction

Syngas (CO/H_2), a pivotal platform for chemical synthesis, was projected to reach a global production capacity exceeding 290.9 million Nm^3 per h in 2025.[1] Dry reforming of methane (DRM) represents a particularly promising route for syngas production, offering the dual advantages of reducing carbon emissions and supplying valuable feedstock.[2–6] However, using conventional catalysts, competitive adsorption/activation of CH_4 and CO_2 at the catalyst surface invariably leads to preferential conversion of one reactant, with the H_2 : CO ratio deviating from unity.[7–11] As illustrated in Fig. 1a, excessive CH_4 adsorption and decomposition lead to elevated H_2 : CO ratios (>1) and severe carbon deposition, causing catalyst deactivation.[7,12,13] Conversely, predominant CO_2 chemisorption triggers the reverse water-gas shift (RWGS) reaction, resulting in sub-stoichiometric H_2 : CO ratios (<1) and compromised hydrogen utilization.[11,14–17] Therefore, the rational design of catalysts that can balance CH_4 and CO_2 activation is essential to realize near-stoichiometric DRM, enabling durability and industrial-scale application.

A temporal decoupling strategy, chemical looping DRM, has been developed to address competitive adsorption by separating CH_4 oxidation and CO_2 reduction into alternating steps over oxygen-storage materials (Fig. 1b).[18–20] This approach effectively suppresses coking formation and avoids RWGS, enabling near-stoichiometric H_2 : CO ratios (~1). Despite this promise, the practical implementation of chemical looping DRM suffers from inherent drawbacks, including energy-intensive temperature swings, reliance on inert gas purging for phase separation, and sluggish kinetics of oxygen mobility in oxygen storage materials, collectively hindering scalability and operational flexibility.

Herein, we report a rationally designed catalyst featuring dual-active sites of Pt clusters and frustrated Lewis pairs (FLPs) (Fig. 1c), where CH_4 oxidation and CO_2 reduction proceed concurrently yet remain spatially segregated on distinct catalytic sites, subsequently coupling through *O migration across the CeO_2 support. The FLP sites on CeO_2(110), composed of adjacent Ce^{3+} Lewis acids paired with a neighbouring lattice O^{2-} Lewis base (Fig. 1c),[21] exhibit exceptional CO_2 adsorption and activation, outperforming conventional oxygen vacancies and metal–CeO_2 interfaces. This enables spatial decoupling of CO_2 reduction from CH_4 dissociation on Pt clusters. Mechanistically, CO_2 reduction at FLP sites directly generates CO and reactive *O species; the *O then migrates rapidly across the CeO_2 surface to Pt clusters, where it drives the partial oxidation of CH_4 to H_2 and CO (Fig. 1c). This dynamic coupling affords a near-stoichiometric H_2 : CO ratio of 0.99, which in turn delivers exceptional catalytic stability (>400 h) with a turnover number exceeding 7 200 000. Moreover, the catalyst achieves a remarkable CH_4 conversion rate of 93.9 mol g_{Pt}^{-1} h^{-1} at 700 °C, surpassing recently reported state-of-the-art systems.

School of Chemistry and Chemical Engineering, Northwestern Polytechnical University, 710072 Xi'an, China. E-mail: zhangsai1112@nwpu.edu.cn; yongquan@nwpu.edu.cn

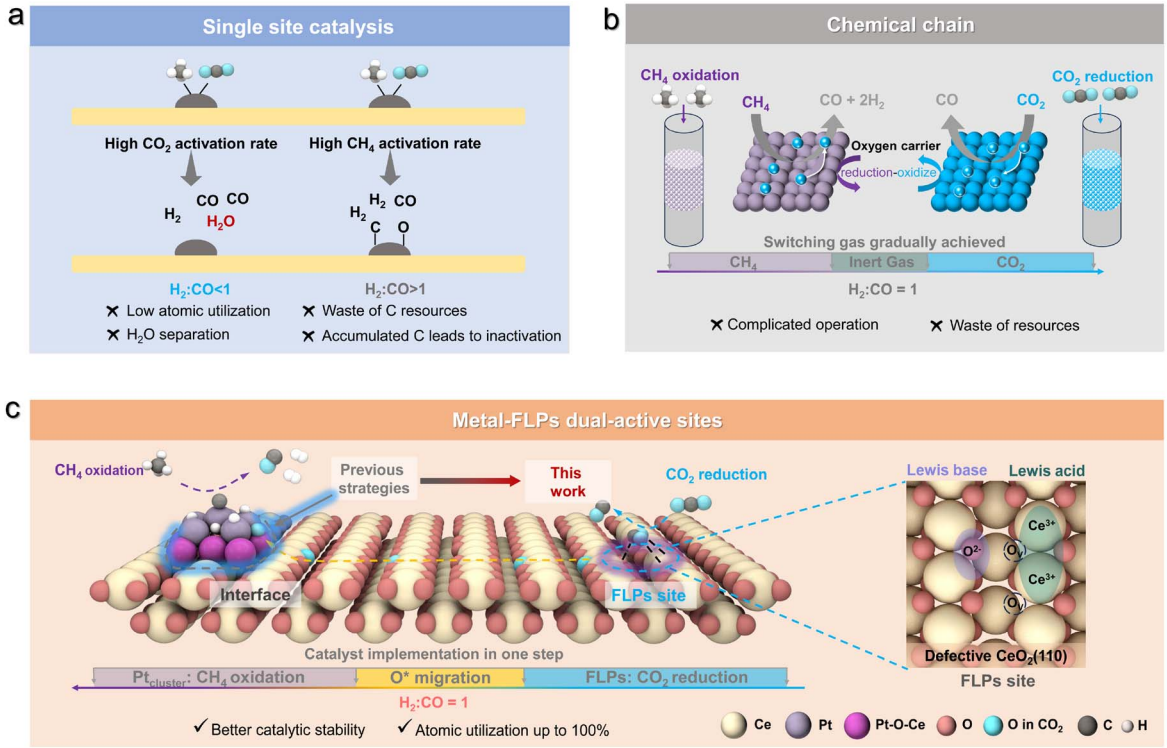

Fig. 1 Spatially decoupled CO_2 reduction and CH_4 oxidation. (a) Schematic diagram highlighting the inherent limitations of conventional DRM catalysts. (b) Schematic diagram of chemical looping DRM, achieving separation of CO_2 reduction and CH_4 oxidation. (c) Conceptual illustration of the spatially decoupled CH_4 oxidation and CO_2 reduction on the Pt clusters and FLP sites, respectively, mediated through oxygen spillover.

Results and discussion

Theoretical investigation and catalytic performance

Ceria (CeO_2) serves as an ideal oxygen storage component owing to its exceptional redox properties and defect-engineered surface chemistry, which facilitates facile oxygen mobility within its lattice.[22–24] However, the nonpolar C–H bonds of CH_4 resist activation on the Lewis acid/base pairs of CeO_2, necessitating metal sites where d-orbitals facilitate the requisite electron transfer for C–H scission.[17,25–28] In contrast, CO_2 adsorption is efficiently promoted at the metal–CeO_2 interface.[29–31] To achieve spatially decoupled catalysis, we reasoned that the CeO_2 supports must possess sites with exceptionally strong and selective affinity for CO_2, thereby isolating its activation from CH_4 oxidation on metal sites and preventing *H intermediates from triggering the deleterious RWGS reaction.

Density functional theory (DFT) calculations were employed to guide this design. As shown in Fig. 2a and S1–S5, CO_2 adsorption at the oxygen vacancy (O_V) on CeO_2(110) (CeO_2(110)-O_V) is significantly stronger than that on CeO_2(111)-O_V, with an adsorption energy of −2.51 eV. Although this value is more negative than that for CO_2 adsorption on Pt_6 clusters, it remains comparable to that at the Pt_6–CeO_2 interface, indicating that an isolated O_V is insufficient to achieve the full spatial decoupling. Notably, constructing adjacent O_V pairs on CeO_2(110) creates the FLP sites (Ce^{3+}…Ce^{3+}, O^{2-}; Fig. 2b), which dramatically enhance CO_2 adsorption, with an energy of −3.30 eV (Fig. 2a). In contrast, creating more O_Vs on CeO_2(111) merely increases the number of O_Vs without creating a distinct adsorption site (Fig. 2b). These results confirm that a FLP on CeO_2(110), coupled with Pt clusters, provides an ideal platform for spatially decoupled catalysis toward efficient and stoichiometric DRM.

Guided by the above analysis, we synthesized porous CeO_2 nanorods (denoted as CeO_2-FLP) designed to host FLP sites through a sequential low- and high-pressure hydrothermal method.[21,32] Dark-field transmission electron microscopy (TEM) images revealed a well-defined porous architecture with an average pore size of 2–3 nm (Fig. S6a). High-resolution TEM showed lattice fringes with a lattice fringe spacing of 0.19 nm, corresponding to the CeO_2 [220] planes (Fig. S6b), indicating the preferential growth along the [110] direction. X-ray photoelectron spectroscopy (XPS) analysis of Ce 3d and O 1s peaks indicated the abundance of surface defects in CeO_2-FLP, as evidenced by the Ce^{3+} (29.4%, Fig. S7a) and Ce^{3+}-O (52.4%, Fig. S7b) fractions. The abundance of O_V, along with the exposure of (110) facets, suggests the effective formation of FLP sites on the CeO_2-FLP surface.[21,33,34]

Subsequently, Pt clusters were deposited on CeO_2-FLP ($Pt_{cluster}$/CeO_2-FLP) using $H_2PtCl_6 \cdot 6H_2O$ as the precursor *via* a photo-assisted reduction process. The actual Pt loading was quantified to be 0.9 wt% using inductively coupled plasma optical emission spectroscopy (ICP-OES). High-angle annular dark-field scanning transmission electron microscopy (HAADF-STEM) images of $Pt_{cluster}$/CeO_2-FLP revealed brightness variation on CeO_2-FLP (Fig. 2c), indicating the presence of Pt clusters

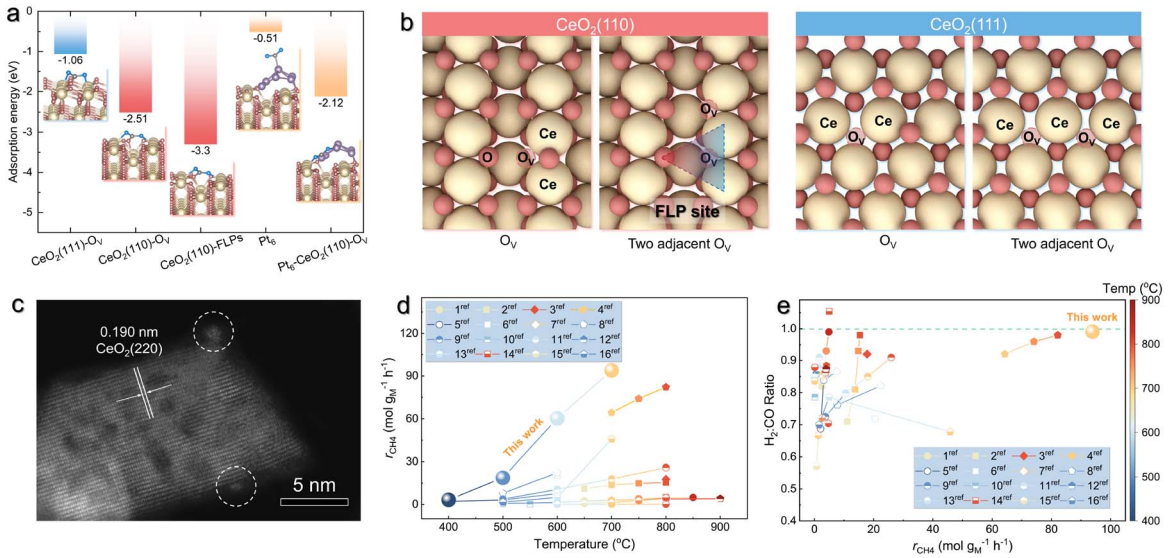

Fig. 2 Theoretical investigation and catalytic performance. (a) The CO_2 adsorption behaviors on the CeO_2(110) surface with various active sites. (b) Optimized structure of one O_V and two adjacent O_Vs on CeO_2(110) and CeO_2(111) surfaces. (c) HAADF-STEM image of $Pt_{cluster}/CeO_2$-FLP. (d) Comparison of CH_4 conversion rates over $Pt_{cluster}/CeO_2$-FLP and other state-of-the-art catalysts (see Table S2 for more details). (e) Comparison of CH_4 conversion rates and H_2 : CO ratios over $Pt_{cluster}/CeO_2$-FLP and other state-of-the-art catalysts under similar reaction conditions (see Table S2 for more details).

with an average size of 0.9 ± 0.1 nm (Fig. S8). CO chemical adsorption determined a Pt dispersion of 43.2% (Table S1). Importantly, $Pt_{cluster}/CeO_2$-FLP retained high Ce^{3+} (30.9%) and Ce^{3+}-O (55.2%) fractions (Fig. S7), confirming the preservation of the FLP-rich surface.

The DRM performances of $Pt_{cluster}/CeO_2$-FLP were evaluated in a fixed-bed reactor at a feed ratio of $CH_4 : CO_2 : N_2$ (2 : 2 : 1). At 700 °C, $Pt_{cluster}/CeO_2$-FLP achieved a CH_4 conversion of 75.7% (Fig. S9), approaching the thermodynamic equilibrium (76.0%, at 700 °C), along with a CH_4 conversion rate of 93.9 mol g_{Pt}^{-1} h^{-1}. This activity substantially exceeds that of state-of-the-art catalysts (Fig. 2d and Table S2). Importantly, the H_2 and CO production rates reached 187.7 mol g_{Pt}^{-1} h^{-1} and 189.5 mol g_{Pt}^{-1} h^{-1}, respectively, giving a near-stoichiometric H_2 : CO ratio of 0.99. Therefore, $Pt_{cluster}/CeO_2$-FLP delivers an unprecedented combination of high activity and ideal product stoichiometry for DRM (Fig. 2e and Table S2).

Critical functions of the FLP sites

As a catalyst design concept (Fig. 1c), the FLP sites on the CeO_2(110) surface, rather than Pt clusters or Pt–CeO_2 interfaces, are responsible for the strong CO_2 adsorption and activation. This capability is absent on the CeO_2(111) facet, theoretically leading to inferior DRM performance. We synthesized nano-octahedral CeO_2 (denoted as CeO_2-O_V) exclusively exposing (111) facets, which are structurally incompatible with FLP formation and thus possess only conventional O_V (Fig. 2b and S10).[21] Consistent with this morphology, CeO_2-O_V exhibited a lower concentration of surface defects, with Ce^{3+} and Ce^{3+}-O_V fractions of 19.3% and 40.3%, respectively (Fig. S11 and Table S1). Using the same photo-assisted deposition method, Pt clusters were loaded onto CeO_2-O_V ($Pt_{cluster}/CeO_2$-O_V) at 1.1 wt% loading. HAADF-STEM image confirmed the Pt clusters with an average size of 0.9 ± 0.3 nm (Fig. 3a and S12). Meanwhile, Pt deposition did not substantially alter the surface defect of CeO_2-O_V, with Ce^{3+} and Ce^{3+}-O fractions remaining at 20.4% and 42.4%, respectively (Fig. S11 and Table S1). Under identical reaction conditions, $Pt_{cluster}/CeO_2$-O_V, despite possessing comparable Pt clusters, exhibited markedly inferior DRM performance. Specifically, CH_4 conversion was 35.1% (Fig. 3b), 2.2-fold lower than that of $Pt_{cluster}/CeO_2$-FLP (75.7%) at 700 °C. Meanwhile, the H_2 : CO ratio plummeted to 0.5, indicating severe deviation from stoichiometric product ratios (Fig. 3b). These comparative results unequivocally establish that the FLP sites are essential for achieving exceptional DRM activity and stoichiometry.

Kinetic analysis at low conversions (<20%) further elucidates the critical role of FLP. The CO_2 reaction order over $Pt_{cluster}/CeO_2$-FLP was significantly lower than that over $Pt_{cluster}/CeO_2$-O_V (Fig. 3c), indicating higher CO_2 surface coverage on the FLP-containing catalyst. Arrhenius plots ($\ln k$ *vs.* $1/T$, Fig S13 and S14) revealed that the activation energy (E_a) for CO_2 conversion on CeO_2-FLP (59.6 kJ mol^{-1}) was substantially lower than that on CeO_2-O_V (79.1 kJ mol^{-1}). Thus, the higher CO_2 coverage on $Pt_{cluster}/CeO_2$ results in the stronger conversion capacity, directly distinguishing FLP from O_Vs. This trend was further supported by CO_2 temperature-programmed desorption (CO_2-TPD, Fig. S15), in which CeO_2-FLP displayed an additional strong desorption peak at ~500 °C, confirming enhanced CO_2 adsorption at the FLP sites.

More importantly, introducing Pt clusters onto CeO_2-O_V significantly reduced the E_a for CO_2 conversion from 79.1 kJ mol^{-1} (CeO_2-O_V) to 71.5 kJ mol^{-1} ($Pt_{cluster}/CeO_2$-O_V, Fig. S14). In the absence of FLP sites on CeO_2 supports, CO_2 adsorption and

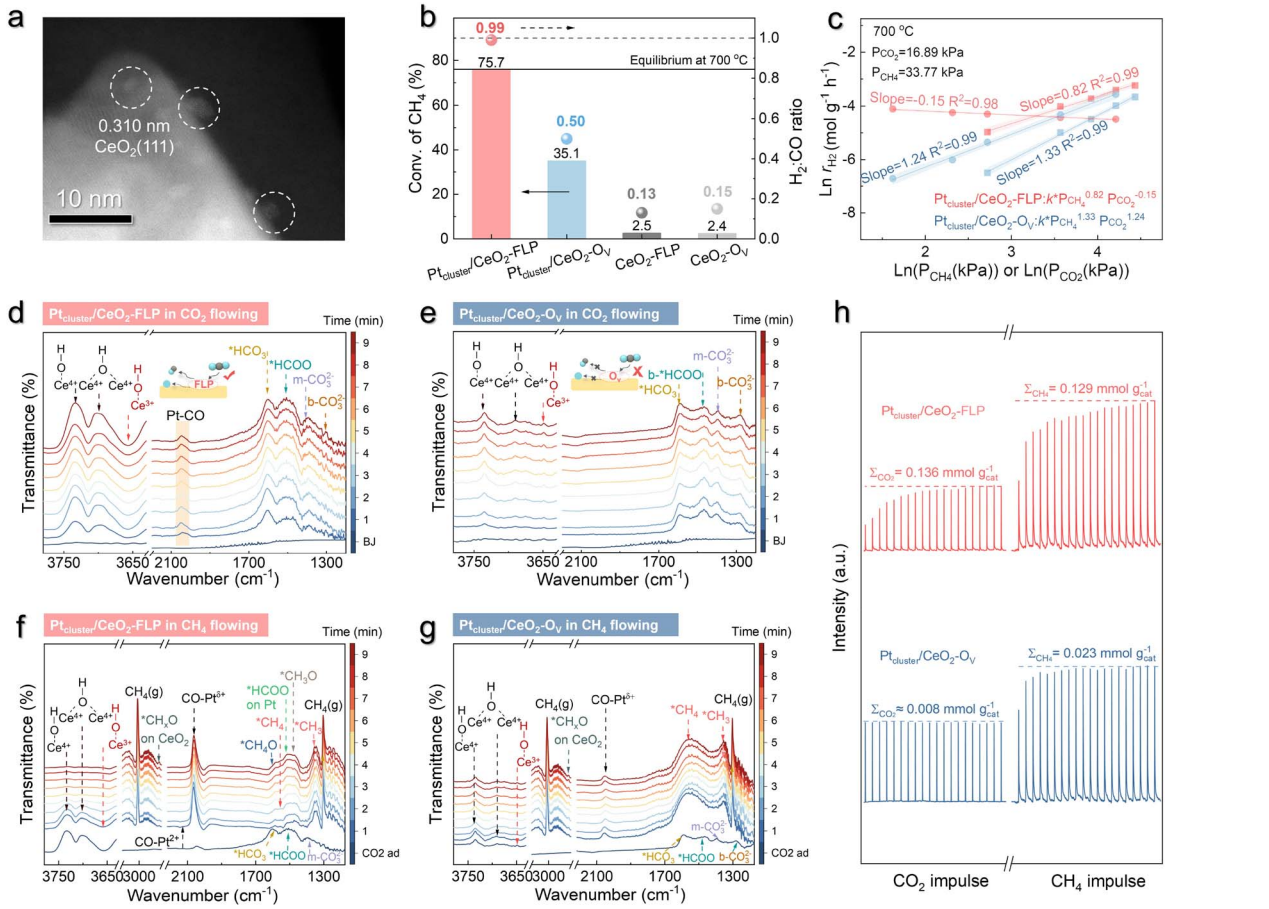

Fig. 3 Investigations on the critical functions of FLP. (a) HAADF-STEM image of $Pt_{cluster}/CeO_2$-O_V. (b) CH_4 conversions and H_2/CO ratios at 700 °C with a WHSV of 30 000 mL g_{cat}^{-1} h^{-1}. (c) Kinetic measurements of $Pt_{cluster}/CeO_2$-FLP and $Pt_{cluster}/CeO_2$-O_V. *In situ* DRIFTS spectra of (d) $Pt_{cluster}/CeO_2$-FLP and (e) $Pt_{cluster}/CeO_2$-O_V under CO_2 flow. *In situ* DRIFTS spectra of (f) $Pt_{cluster}/CeO_2$-FLP and (g) $Pt_{cluster}/CeO_2$-O_V under CH_4 flow after CO_2 flow. Note: all of the catalysts were pre-treated by Ar flow for 30 min. Initially, a flow of 50 vol.% CO_2/Ar was introduced and the DRIFTS signals were collected at 350 °C every 1 min. Subsequently, the 50 vol.% CO_2/Ar gas was switched to a flow of 50 vol.% CH_4/Ar. The DRIFTS signals were further collected at 350 °C every 1 min. (h) Pulsed reactions of CO_2 and CH_4 over $Pt_{cluster}/CeO_2$-FLP and $Pt_{cluster}/CeO_2$-O_V.

activation are influenced by Pt or the Pt–CeO_2 interface, consistent with previous reports. Conversely, depositing Pt onto CeO_2-FLP exhibited a negligible effect on the E_a for CO_2 conversion, as evidenced by the nearly identical values for $Pt_{cluster}/CeO_2$-FLP (55.7 kJ mol^{-1}) and CeO_2-FLP (59.6 kJ mol^{-1}; Fig. S14). Different form conventional O_V sites, these kinetic results experimentally demonstrate that CO_2 activation occurs predominantly on FLP sites rather than at Pt clusters or the Pt–O–Ce interfaces, with Pt clusters playing a negligible direct role in CO_2 transformation.

Subsequently, *in situ* diffuse reflectance infrared Fourier transform spectroscopy (DRIFTS) was employed to monitor the roles of FLP under the given reaction conditions. Both $Pt_{cluster}/CeO_2$-FLP (Fig. 3d) and $Pt_{cluster}/CeO_2$-O_V (Fig. 3e) exhibited characteristic vibrational signatures of bicarbonate (*HCO_3, at 1602 cm^{-1}) and formate (*HCOO, 1505 cm^{-1}) intermediates, confirming the CO_2 chemisorption on CeO_2 supports.[35,36] However, $Pt_{cluster}/CeO_2$-FLP exhibited strong capacity of transformation of b-CO_3^{2-}, as evidenced from their much weaker adsorption peaks at ~1300 cm^{-1}. Furthermore, $Pt_{cluster}/CeO_2$-FLP displayed an obvious *CO adsorption band (~2046 cm^{-1}) associated with Pt clusters, which was not detected on $Pt_{cluster}/CeO_2$-O_V. This critical distinction confirms that CeO_2-FLP enables a direct CO_2-to-CO reduction pathway.[37,38] Moreover, during CO_2 exposure on $Pt_{cluster}/CeO_2$-FLP, the Ce^{3+}-OH stretching mode (~3656 cm^{-1}) attenuated while Ce^{4+}-OH features (~3733 cm^{-1} and ~3698 cm^{-1}) intensified (Fig. 3d and e),[39–41] indicating the accumulation of *O species within the CeO_2-FLP lattice during the CO_2-to-CO reduction, accompanied by the Ce^{3+}-to-Ce^{4+} oxidation.

When a CH_4 flow was introduced into the *in situ* reactor, $Pt_{cluster}/CeO_2$-FLP exhibited a significantly enhanced intensity of *CO adsorption on Pt clusters, indicating that the CH_4 oxidation occurred on the Pt sites (Fig. 3f). Meanwhile, the vibrational features corresponding to the *CH_3 (~1342 cm^{-1}), *CH_3O (~1471 cm^{-1}), *CH_4O (~1583 cm^{-1}) and Pt-bound *HCOO (~1517 cm^{-1}) species emerged during CH_4 flow, along with the disappearance of CeO_2-bound *HCOO bonding (~1509 cm^{-1}) and *CO_3^{2-} (~1397 cm^{-1}) intermediates. Simultaneously, the Ce^{4+} species (Ce^{4+}-OH, 3733 cm^{-1}) was reduced to

Ce^{3+} (Ce^{3+}-OH, 3658 cm^{-1}) along with these transformations. Thus, these findings collectively demonstrate that CH_4 oxidation is mediated by lattice *O species originating from CeO_2-FLP supports.

In contrast, $Pt_{cluster}/CeO_2$-O_V exhibited negligible activity for this reaction pathway (Fig. 3g). The CH_4 exposure on $Pt_{cluster}/CeO_2$-O_V induced the rapid emergence of *CH_3 (at ~1342 cm^{-1}) and *CH_4 (at ~1557 cm^{-1}) species, indicating that CH_4 adsorption and activation occurred on Pt sites.[42,43] However, CO production remained consistently low, demonstrating limited further oxidation of activated *CH_3 and *CH_4 species to *CO. Furthermore, the partial retention of Ce^{4+} species (Ce^{4+}-OH, 3733 cm^{-1}) indicated the restricted *O migration during CH_4 flow, owing to the poor capacity for CO_2 activation/reduction of CeO_2-O_V. Concomitantly, the disappearance of *HCO_3, *HCOO, and b-CO_3^{2-} species could be attributed to the *H spillover from Pt into the CeO_2-O_V supports.

Sequential CO_2/CH_4 pulse experiments further quantified the FLP functions. $Pt_{cluster}/CeO_2$-FLP showed distinct CO_2 consumption over 14 pulse cycles, corresponding to an *O storage capacity of 0.136 mmol g_{cat}^{-1}. This observation contrasted sharply with $Pt_{cluster}/CeO_2$-O_V, which exhibited a negligible *O storage capacity (0.008 mmol g_{cat}^{-1}), consistent with *in situ* DRIFTS spectra confirming only adsorption of CO_2 on CeO_2-O_V (Fig. 3h). Subsequent CH_4 pulses revealed drastically higher consumption on $Pt_{cluster}/CeO_2$-FLP (0.129 $mmol_{CH4}$ g_{cat}^{-1}) than that on $Pt_{cluster}/CeO_2$-O_V (0.023 $mmol_{CH_4}$ g_{cat}^{-1}). The close match between CH_4 consumption and *O storage on $Pt_{cluster}/CeO_2$-FLP confirms efficient transfer of the FLP-generated *O species to Pt sites for CH_4 oxidation.

Investigation into the functions of Pt clusters

Notably, the pronounced reduction in E_a for CH_4 conversion upon introducing Pt clusters ($Pt_{cluster}/CeO_2$-FLP and CeO_2-FLP, 64.1 kJ mol^{-1} and 112.6 kJ mol^{-1}, respectively; $Pt_{cluster}/CeO_2$-O_V and CeO_2-O_V, 79.2 kJ mol^{-1} and 117.2 kJ mol^{-1}, respectively; Fig. S14) unambiguously underscores the essential roles of Pt in CH_4 adsorption and C–H bond activation. Moreover, the comparable CH_4 reaction orders observed on both $Pt_{cluster}/CeO_2$-FLP and $Pt_{cluster}/CeO_2$-O_V indicated that CH_4 activation kinetics were weakly influenced by CeO_2 (Fig. 3c). Taken together, the higher reaction orders and activation energies associated with CH_4 conversion indicated that CH_4 activation constitutes the rate-determining step in the DRM reaction over $Pt_{cluster}/CeO_2$-FLP, particularly under preconditions where CO_2 is efficiently activated by FLP.

To further decipher the mechanistic roles of Pt species in CH_4 activation, the single-atom Pt and Pt nanoparticles (average size 2.2 ± 0.1 nm) were deposited on CeO_2-FLP, yielding Pt_1/CeO_2-FLP (Fig. S16) and Pt_{NP}/CeO_2-FLP (Fig. S17), respectively. ICP-OES determined Pt loadings of 0.5 wt% for Pt_1/CeO_2-FLP and 1.0 wt% for Pt_{NP}/CeO_2-FLP. Notably, the surface properties of the supports in Pt_1/CeO_2-FLP and Pt_{NP}/CeO_2-FLP were similar to those of $Pt_{cluster}/CeO_2$-FLP (Fig. S18 and Table S1), enabling the systematic investigations of Pt speciation effects on CH_4 activation while excluding the influences of supports.

The Pt L_3 edge X-ray absorption near-edge structure (XANES) was used to investigate the electronic states of Pt. The white line peak of Pt_1/CeO_2-FLP was located at 11 567.4 eV, close to that of PtO_2 (Fig. 4a). The k^3-weight Fourier transforms of extended X-ray absorption fine structure (EXAFS) spectra of Pt_1/CeO_2-FLP delivered one prominent peak at ~1.64 Å, which was labeled as the Pt–O bond (Fig. 4b and S19). The lack of Pt–Pt coordination confirmed the atomically dispersed Pt supported on CeO_2-FLP. The wavelet transform analysis directly revealed the absence of Pt–Pt bonds in Pt_1/CeO_2-FLP (Fig. 4c). In contrast, $Pt_{cluster}/CeO_2$-FLP and Pt_{NP}/CeO_2-FLP exhibited the white line peaks between Pt foil and PtO_2 (Fig. 4a), indicating the mixed valence states of Pt. Meanwhile, both Pt–Pt and Pt–O bonds were clearly observed from the k^3-weight Fourier transforms of EXAFS spectra. Compared to Pt_{NP}/CeO_2-FLP, the higher white line peak revealed more amount of the Pt–O bond in $Pt_{cluster}/CeO_2$-FLP, which could be clearly observed from the wavelet transform analysis. Quantitatively, Pt_1/CeO_2-FLP, $Pt_{cluster}/CeO_2$-FLP and Pt_{NP}/CeO_2-FLP exhibited the Pt–O fractions of 100%, 45.4% and 24.2%, respectively, as well as the Pt–Pt fractions of 0%, 54.6% and 75.8%, respectively (Table 1).

For the DRM reaction, $Pt_{cluster}/CeO_2$-FLP, featuring the co-existence of Pt–O and Pt–Pt bonds, delivered the highest CH_4 conversion rate compared to Pt_1/CeO_2-FLP and Pt_{NP}/CeO_2-FLP (Fig. 4d and S20), as well as the lowest E_a of 64.1 kJ mol^{-1} for CH_4 conversion (Fig. 4e and S21). These observations confirm that the highest intrinsic activity of Pt clusters originates from a synergistic interplay between Pt–Pt and Pt–O bonds in CH_4 activation. This synergy arises from the presence of coordinatively unsaturated metal and oxygen on the Pt surface, which promotes the formation of the adsorbed CH_4 σ-complexes and then facilitates C–H bond cleavage in the complexes.[25,44] Furthermore, due to the similar surface properties of supports, all Pt/CeO_2-FLP catalysts exhibited comparable E_a values for CO_2 conversion (Fig. 4e), further confirming the strong capacity of FLP for CO_2 adsorption/activation and the negligible influence of Pt active sites on this process.

The CH_4 activation on Pt/CeO_2-FLP was further investigated by CH_4 temperature-programmed reduction (CH_4-TPR). After the pre-treatment with Ar purging, a CH_4 flow was introduced to probe the catalyst surface. The CeO_2-FLP supports alone exhibited no detectable activation peaks (Fig. S22), further confirming that the CH_4 adsorption and activation occur exclusively at Pt sites. Importantly, $Pt_{cluster}/CeO_2$-FLP exhibited the strongest peak intensity and the lowest initiation temperature compared to both Pt_1/CeO_2-FLP and Pt_{NP}/CeO_2-FLP (Fig. S22). These observations directly confirmed the highest capacity of $Pt_{cluster}/CeO_2$-FLP for the CH_4 adsorption and activation in DRM.

Subsequently, *in situ* DRIFTS experiments were performed to compare the behaviors of Pt clusters and nanoparticles under the given reaction conditions. Under CO_2 flow, Pt_{NP}/CeO_2-FLP exhibited spectral changes nearly identical to those of $Pt_{cluster}/CeO_2$-FLP, consistent with their similar CeO_2 surface properties for CO_2 adsorption (Fig. 4f). Upon switching to CH_4 flow, characteristic peaks corresponding to adsorbed *CH_4 (1557 cm^{-1}) appeared on Pt_{NP}/CeO_2-FLP, confirming CH_4 adsorption

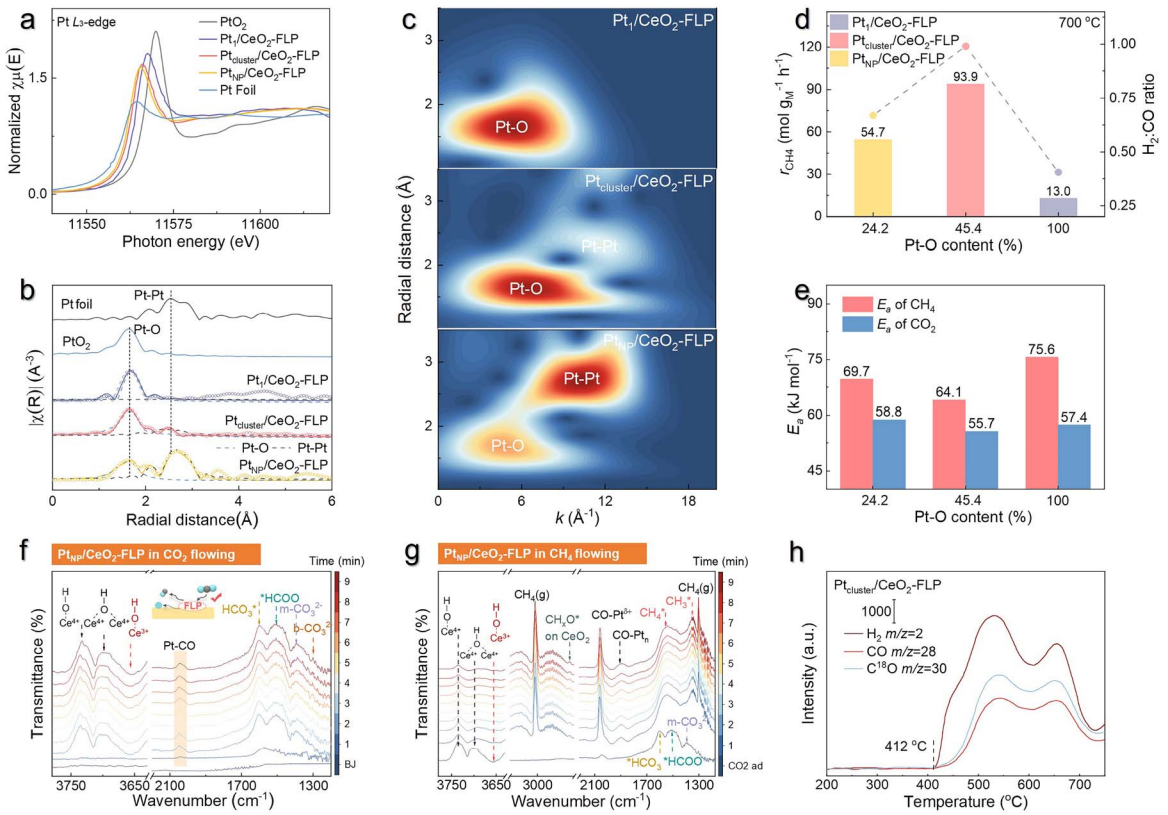

Fig. 4 Investigation on the functions of Pt clusters. (a) XANES spectra of Pt foil, $Pt_{cluster}/CeO_2$-FLP, Pt_1/CeO_2-FLP, Pt_{NP}/CeO_2-FLP and PtO_2. (b) The k^3 weighted Fourier-transformed spectra derived from the EXAFS spectra. (c) Wavelet-transform plots by using the k^3 space. (d) Direct correlation between Pt–O bond contents and CH_4 conversion rates/H_2 : CO ratios. (e) Plots of Pt–O bond contents *vs.* calculated E_a values of $Pt_{cluster}/CeO_2$-FLP, Pt_1/CeO_2-FLP, and Pt_{NP}/CeO_2-FLP for DRM. *In situ* DRIFTS spectra of Pt_{NP}/CeO_2-FLP under (f) CO_2 flow and (g) CH_4 flow after CO_2 flow. Note: all of the catalysts were pre-treated by a flow of Ar for 30 min. Then, a flow of 50 vol.% CO_2/Ar was introduced and the DRIFTS signals were collected at 350 °C every 1 min. Subsequently, the 50 vol.% CO_2/Ar gas was switched to a flow of 50 vol.% CH_4/Ar. The DRIFTS signals were further collected at 350 °C every 1 min. (h) *In situ* mass spectrometry analysis of the temperature-programmed CH_4 oxidation of $Pt_{cluster}/CeO_2$-FLP upon pre-treatment with $H_2{}^{18}O$.

Table 1 Fitting results of EXAFS for Pt_1/CeO_2-FLP, $Pt_{cluster}/CeO_2$-FLP and Pt_{NP}/CeO_2-FLP[a]

Sample	Paths	N^b	R (Å)^c	σ^2 ($\times10^{-3}$ Å^2)^d	$S_0{}^2$	E_0 (eV)	R Factor
Pt foil	Pt–Pt	12.0	2.77	—	—	—	—
PtO_2	Pt–O	6.0	2.07	—	—	—	—
Pt_1/CeO_2-FLP	Pt–O	3.4 ± 0.1	2.04 ± 0.07	5.2 ± 0.9	0.8	7.4	0.018
$Pt_{cluster}/CeO_2$-FLP	Pt–O	4.4 ± 0.4	2.07 ± 0.02	2.1 ± 0.2	0.8	8.5	0.012
	Pt–Pt	5.3 ± 0.5	2.82 ± 0.16	5.2 ± 0.1			
Pt_{NP}/CeO_2-FLP	Pt–O	3.0 ± 0.7	2.10 ± 0.03	7.0 ± 2.9	0.8	8.7	0.008
	Pt–Pt	9.4 ± 0.2	2.78 ± 0.14	5.8 ± 0.6			

[a] The data ranges used in the fit are $2.0 \leq k \leq 13.0$ Å^{-1} and $1.2 \leq R \leq 3.5$ Å, and depend on the quality of data. The number of fitted variable parameters was 10, which was smaller than the total number of independent data points, approximately 16.1. R-Factors for these fittings are all below 0.02. [b] Average coordination number. The half path length. [c] The paths for Pt–O, Pt–Pt are from the crystal structure of PtO_2 ($P6_3mc$) and Pt ($Fm\bar{3}m$). [d] Debye–Waller factor.

(Fig. 4g). Unlike $Pt_{cluster}/CeO_2$-FLP, no clear signals for $*CH_xO$ intermediates were detected on Pt_{NP}/CeO_2-FLP. Moreover, the Ce^{4+}-OH peak persisted even after 9 min CH_4 flow, indicating restricted *O migration from the support to the Pt nanoparticles. Together with CH_4-TPR results, these observations demonstrate that Pt clusters uniquely promote the migration of *O species, which in turn enhances CH_4 activation and overall DRM activity.

Building on the foregoing analysis, the spatially separated Pt clusters and FLP sites serve distinct roles in CH_4 oxidation and CO_2 reduction, respectively, with *O migration acting as the key coupling step, as illustrated in Fig. 1c. To further probe the

origin and transfer of *O species, we performed ^{18}O-isotope labeling experiments. Because labeled CO_2 can lead to ambiguity from residual adsorption or desorption of ^{18}O-containing species, we designed the experiment using $H_2{}^{18}O$ pretreatment, which readily dissociates on CeO_2 but not on Pt clusters.[32,45,46] Specifically, after pretreating $Pt_{cluster}/CeO_2$-FLP with $H_2{}^{18}O$ at 150 °C for 30 min, purging with Ar for 30 min was performed to remove physically adsorbed species. The programmed temperature increase of CH_4 oxidation from 200 °C to 750 °C (10 vol.% CH_4/He, 50 mL min^{-1}) revealed the appearance of the $C^{18}O$/CO signal (Fig. 4h), which directly demonstrated that *O species stored in the CeO_2-FLP support participate in CH_4 oxidation through oxygen transfer to Pt clusters. Furthermore, the H_2 signal appears simultaneously with the CO/$C^{18}O$ signals, indicating that CH_4 dissociates on Pt sites, with CO and H_2 formation. Notably, the observed $C^{18}O$ signal indicates that the oxygen involved in CH_4 oxidation originated predominantly from $H_2{}^{18}O$-derived $*^{18}O$ species stored in the CeO_2-FLP support rather than from the lattice oxygen. Together, these results strongly support a spatially decoupled reaction pathway in which *O migration couples CO_2 reduction on the support with CH_4 oxidation on Pt clusters.

Activity matching between Pt clusters and FLP sites

Achieving activity balance between the spatially decoupled CO_2 reduction and CH_4 oxidation is critical for high-performance DRM under the *O migration coupling process, as it ensures near stoichiometric H_2 : CO ratios (1 : 1) and long-term catalytic stability. As shown in Fig. 5a, this activity balance is inherently determined by the quantitative relationship between FLP sites (responsible for CO_2 reduction) and Pt clusters (mediating CH_4 oxidation). While the FLP sites remain fixed within the CeO_2-FLP supports, we precisely adjusted the number of Pt centers by controlling the Pt loadings. HAADF-STEM images revealed that increasing Pt loadings from 0.5 wt% to 2.0 wt% enhanced the densities of Pt clusters while preserving their similar cluster dimensions (an average diameter of 0.9–1.0 nm, Fig. S23). This controlled variation in Pt cluster population enabled systematic modulation of the FLP-to-Pt site ratios, a crucial factor governing overall DRM performance.

For DRM, Pt loading significantly influenced reaction kinetics and product stoichiometry. At 0.5 wt% Pt loading, the CH_4 conversion rate of 115.7 mmol $g_{cat}{}^{-1}$ h^{-1} was lower than the CO_2 conversion rate of 169.7 mmol $g_{cat}{}^{-1}$ h^{-1}, resulting in

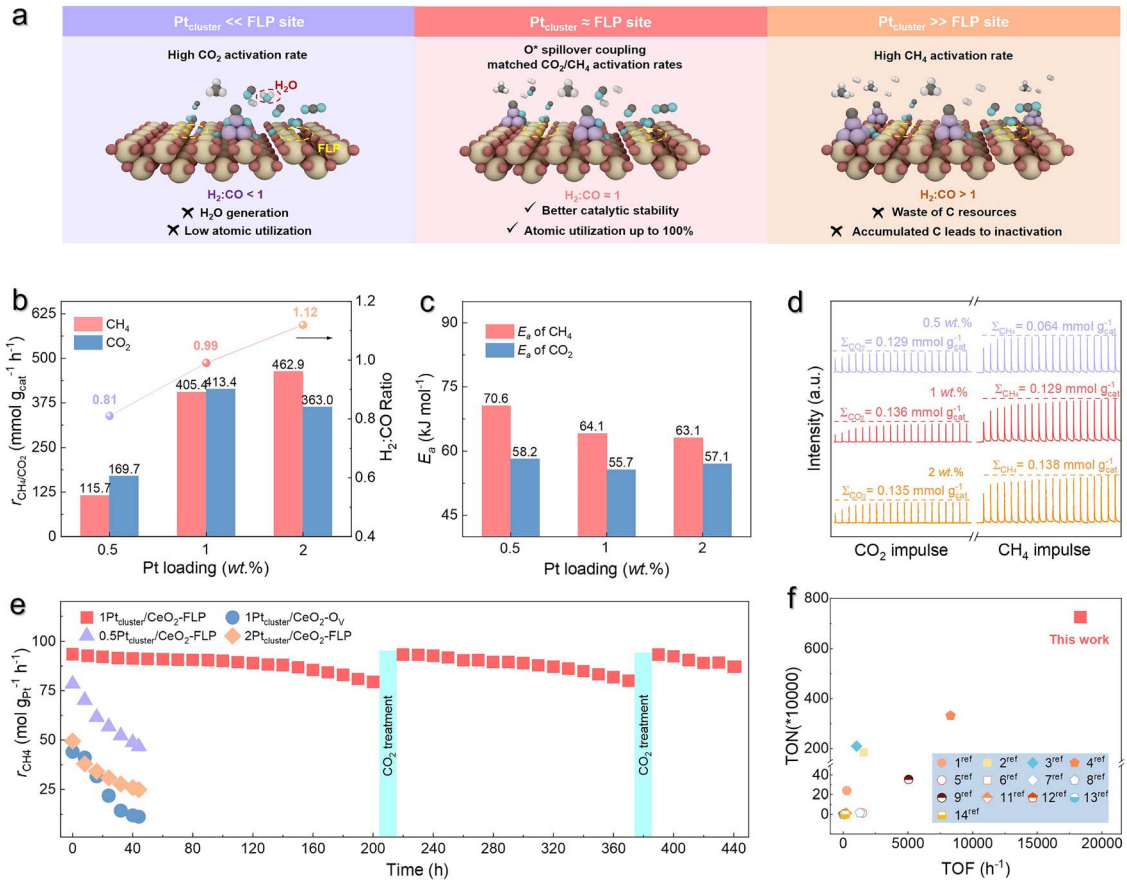

Fig. 5 Activity matching. (a) Scheme of activity matching between Pt clusters and FLPs for the DRM reaction. (b) Influences of Pt loadings on the CH_4/CO_2 generation rates and H_2 : CO ratios of the $Pt_{cluster}/CeO_2$-FLP catalysts for DRM. (c) Influence of Pt loadings on the E_a values of $Pt_{cluster}/CeO_2$-FLP for CO_2 and CH_4 conversions. (d) Pulsed reactions of CO_2 and CH_4 over $Pt_{cluster}/CeO_2$-FLP with various Pt loadings. (e) Catalytic stability of various catalysts with a WHSV of 30 000 mL $g_{cat}{}^{-1}$ h^{-1} (CH_4 : CO_2 : N_2 = 2 : 2 : 1) at 700 °C. CO_2 treatment conditions: CO_2/N_2 at 700 °C for 10 h with a WHSV of 18 000 mL $g_{cat}{}^{-1}$ h^{-1}. (f) Comparison of TON and TOF between $Pt_{cluster}/CeO_2$-FLP and other state-of-the-art catalysts under similar reaction conditions (see Table S2 for more details).

a significantly reduced $H_2:CO$ ratio of 0.81 at 700 °C (Fig. 5b and S24). Elevating the Pt loading to 1 wt%, accompanied with a higher density of Pt clusters, drastically improved the enhanced CH_4 conversion rate (405.4 mmol g_{cat}^{-1} h^{-1}), matching the CO_2 conversion rate of 405.6 mmol g_{cat}^{-1} h^{-1}. Simultaneously, the $H_2:CO$ ratio approached 0.99, nearly achieving a stoichiometric ratio of 1 (Fig. 5b). Therefore, increasing the Pt loading facilitated the optimal matching between Pt clusters and FLP sites.

Further increasing the Pt loading to 2 wt% resulted in CH_4 and CO_2 conversion rates similar to those observed for $Pt_{cluster}/CeO_2$-FLP with 1 wt% Pt loading (Fig. 5b and S24). This observation demonstrated that the CH_4 activation and conversion depended on the migration of *O species generated from the CO_2 reduction on FLP of CeO_2-FLP, rather than the availability of Pt clusters. Consequently, CH_4 conversion rates plateau at the 1 wt% Pt loading, as additional Pt clusters cannot compensate for the limited *O supply from the FLP. The extra CH_4 conversion would lead to carbon deposition on the catalyst surface (Fig. 5a). Carbon balance analysis before and after the reaction revealed greater carbon imbalance for $Pt_{cluster}/CeO_2$-FLP with higher Pt loadings, indicating direct carbonization of CH_4 on Pt (Fig. S25). Raman spectroscopy of the spent $Pt_{cluster}/CeO_2$-FLP catalysts proved the direct evidence of carbonaceous species (Fig. S26). After 45 h reaction at 700 °C, thermogravimetric analysis (TGA) quantified a carbon deposition rate of 2.69 mg g_{cat}^{-1} h^{-1} for the 2 wt% $Pt_{cluster}/CeO_2$-FLP catalysts, which was ~7 times higher than that for 1 wt% and 0.5 wt% catalysts (0.39 and 0.38 mg g_{cat}^{-1} h^{-1}, respectively; Fig. S27). Collectively, these results reveal the critical role of the balanced FLP-to-Pt site ratios in achieving efficient DRM performance with stoichiometric $H_2:CO$ output.

Kinetic analysis further clarified the activity matching requirements between Pt clusters and FLP sites (Fig. S28). The comparable E_a values of $Pt_{cluster}/CeO_2$-FLP for CO_2 conversion indicated that CO_2 adsorption and transformation predominantly occurred on FLP sites (Fig. 5c). Theoretically, similar Pt clusters in $Pt_{cluster}/CeO_2$-FLP should yield comparable E_a values for CH_4 conversion. However, when the Pt loading was 0.5 wt%, the relatively large distance between Pt clusters and FLP sites resulted in a higher E_a value for CH_4 conversion. In contrast, sufficient Pt loading (>1.0 wt%) reduces the average spatial distance between Pt clusters and FLP sites, leading to sufficient migration and supply of *O species and thus delivering comparable E_a values for CH_4 conversion. When the number of Pt clusters matched that of FLP sites, the E_a values for CH_4 conversion and CO_2 conversion were also comparable, thereby facilitating the DRM reaction with a near-stoichiometric ratio of $H_2:CO \approx 1$. This kinetic deconvolution highlights the critical roles of the available Pt clusters and FLP sites in balancing *O supply (from FLPs) and CH_4 activation (at Pt) for DRM.

The CO_2 pulse experiments revealed that $Pt_{cluster}/CeO_2$-FLP with varying Pt loadings exhibited comparable *O storage capacities (0.129–0.136 mmol g_{cat}^{-1}, Fig. 5d). These findings further confirm that FLP sites act as active centers for CO_2 reduction, generating reactive *O species that subsequently participate in CH_4 oxidation pathways. Specially, the Pt loading of 0.5 wt% yielded a low rate of 0.043 mmol g_{cat}^{-1} due to the insufficient amount and density of Pt clusters. When the Pt loadings were elevated to 1.0 wt% and 2.0 wt%, the CH_4 consumption increased to 0.129 mmol g_{cat}^{-1} and 0.138 mmol g_{cat}^{-1}, respectively. Excessive Pt loading did not enhance DRM activity, as the FLP sites imposed a kinetic bottleneck of the *O supply from the CO_2 reduction.

Notably, the observed CH_4 consumption over $Pt_{cluster}/CeO_2$-FLP did not scale with the population of Pt clusters as the Pt loading increased from 1.0 wt% to 2.0 wt%, contradicting the scenario where only interfacial oxygen is involved in the reaction. This deviation indicates that the *O species are not confined to the Pt–CeO_2 interface. Instead, the facile migration of oxygen across the CeO_2-FLP support enables the entire oxygen reservoir of the carrier to participate in CH_4 oxidation. Consequently, these findings further demonstrate that CO_2 activation occurs extensively on the FLP sites of CeO_2-FLP, thereby achieving spatial decoupling from CH_4 oxidation at the Pt clusters.

Additionally, the optimal synergy of Pt clusters and FLP sites directly enhances catalytic stability. $Pt_{cluster}/CeO_2$-O_V, lacking FLP sites, exhibited inferior stability, as evidenced by the substantially declined conversions of CH_4 and CO_2 during a period of 45 h (Fig. 5e). Similarly, $Pt_{cluster}/CeO_2$-FLP with either insufficient (0.5 wt%) or excessive (2.0 wt%) Pt loading exhibited compromised durability, attributable respectively to limited CH_4 activation capacity and inadequate *O-migration kinetics. In contrast, the optimally matched $Pt_{cluster}/CeO_2$-FLP (1 wt% Pt loading) catalyst delivered exceptional long-term stability, maintaining nearly constant CH_4 conversion rates (Fig. 5e) and a near-stoichiometric $H_2:CO$ ratio (Fig. S29) for over 400 h. During the initial 100 h, when the H_2/CO ratio remained near 1, no detectable water appeared in the product stream, indicating effective suppression of the RWGS reaction. However, XPS analysis of the spent $Pt_{cluster}/CeO_2$-FLP catalyst revealed both reduced surface defects and accumulated carbonaceous species (Fig. S30), which together mask Pt clusters and FLP sites. Notably, a slight 15% loss in activity during long-term testing was completely reversed by a simple CO_2 treatment (Fig. 5e). This remarkable stability reflected in a turnover number (TON) exceeding 7 200 000 per exposed Pt site for CH_4 conversion (Fig. 5f and S31). To the best of our knowledge, $Pt_{cluster}/CeO_2$-FLP represents the first to simultaneously achieve such a record-high TON and unprecedented activity, with its TON value nearly double the previously reported maximum (Fig. 5f).

Finally, we propose a catalytic process for DRM on $Pt_{cluster}/CeO_2$-FLP that spatially decouples CO_2 reduction and CH_4 oxidation, as illustrated in Fig. 1c. The CO_2 reduction step follows a Mars–van Krevelen (MvK) mechanism: CO_2 is adsorbed and activated at FLP sites, directly forming CO and leaving *O species on the CeO_2-FLP support. Subsequently, the *O species migrate from FLP sites to Pt clusters. On Pt clusters, CH_4 is converted to CO and H_2 *via* *CH_xO intermediates, facilitated by the migrated *O species. Thus, while the individual CO_2 reduction step obeys the classical MvK redox cycle, the overall process represents a modified MvK-type pathway enabled by spatial decoupling and *O migration between distinct active

sites. This design separates CO_2 reduction (FLP sites) from CH_4 oxidation (Pt clusters) and couples them through oxygen spillover. Through precise matching of Pt clusters and FLP sites, the two half-reactions are efficiently coupled, leading to a near-stoichiometric H_2/CO ratio and sustained DRM activity.

Conclusions

In summary, this work demonstrates that *O migration across a spatially decoupled Pt/CeO_2 catalyst enables near-stoichiometric DRM under continuous operation, delivering durable and high-performance DRM catalysis with a stoichiometric H_2 : CO ratio. This catalyst separates the antagonistic adsorption and activation steps: CO_2 is selectively reduced at FLP sites on the CeO_2(110) facet, while CH_4 is partially oxidized on Pt clusters, with *O shuttling dynamically between the two sites. This *O-transport mechanism intrinsically couples the two half-reactions, maintains a balanced redox cycle, and effectively maintains a H_2 : CO ratio of 0.99 while suppressing coke formation and deactivation pathways. As a result, the catalyst delivers a record CH_4 conversion rate of 93.9 mol g_{Pt}^{-1} h^{-1} at 700 °C with stable operation exceeding 400 h under continuous, isothermal conditions. Although the present study employs Pt/CeO_2(110) as a model platform, the underlying principle is not limited to this specific combination. The key requirements are: (i) a reducible oxide support capable of forming FLP sites (adjacent oxygen vacancies) that strongly activate CO_2 and (ii) metal sites (clusters or nanoparticles) that can activate CH_4 and accept migrating *O species. Many earth-abundant metals (*e.g.*, Ni, Co, and Ru) and other reducible oxides (*e.g.*, TiO_2, WO_3, and In_2O_3) are known to exhibit similar oxygen spillover behavior and have been reported to form frustrated Lewis pair-like defects under reducing conditions. Therefore, we anticipate that the spatial decoupling strategy can be extended to more practical catalyst compositions, guided by the design principles established here.

Author contributions

W. L. performed most of the experiments. J. Y., W. G. and Q. G. participated in data analysis. S. Z. and Y. Q. designed the studies and wrote the paper. All authors discussed the results and commented on the manuscript.

Conflicts of interest

There are no conflicts to declare.

Data availability

The data supporting the findings of this study are available in the main text and supplementary information (SI). Supplementary information: experimental details, catalyst synthesis procedures, characterization data, catalytic performance data, kinetic analysis, *in situ* spectroscopic results, computational details, figures and tables. Additional raw data are available from the corresponding author upon reasonable request. See DOI: https://doi.org/10.1039/d6sc03014a.

Acknowledgements

This work was supported by the National Natural Science Foundation of China Young Student Basic Research Project (Doctoral Student) (225B2209) and the Key Project of the Natural Science Basic Research Program of Shaanxi Province (2024JC-TBZC-16).

Notes and references

1 M. Intelligence, Syngas Market Size, Mordor Intelligence, https://www.mordorintelligence.com/industry-reports/syngas-market, accessed 07 July 2025.
2 C. Palmer, D. C. Upham, S. Smart, M. J. Gordon, H. Metiu and E. W. McFarland, *Nat. Catal.*, 2020, **3**, 83–89.
3 Q. Zhu, H. Zhou, L. Wang, L. Wang, C. Wang, H. Wang, W. Fang, M. He, Q. Wu and F.-S. Xiao, *Nat. Catal.*, 2022, **5**, 1030–1037.
4 Y. Song, E. Ozdemir, S. Ramesh, A. Adishev, S. Subramanian, A. Harale, M. Albuali, B. A. Fadhel, A. Jamal, D. Moon, S. H. Choi and C. T. Yavuz, *Science*, 2020, **367**, 777–781.
5 Y. Liu, D. Deng and X. Bao, *Chem*, 2020, **6**, 2497–2514.
6 L. Zhou, J. M. P. Martirez, J. Finzel, C. Zhang, D. F. Swearer, S. Tian, H. Robatjazi, M. Lou, L. Dong, L. Henderson, P. Christopher, E. A. Carter, P. Nordlander and N. J. Halas, *Nat. Energy*, 2020, **5**, 61–70.
7 T. Zhou, X. Li, J. Zhao, L. Luo, Y. Wang, Z. Xiao, S. Hu, R. Wang, Z. Zhao, C. Liu, W. Wu, H. Li, Z. Zhang, L. Zhao, H. Yan and J. Zeng, *Nat. Mater.*, 2025, **24**, 891–899.
8 S. D. Senanayake, J. A. Rodriguez and J. F. Weaver, *Acc. Chem. Res.*, 2020, **53**, 1488–1497.
9 D. Pakhare and J. Spivey, *Chem. Soc. Rev.*, 2014, **43**, 7813–7837.
10 M.-M. Millet, G. Algara-Siller, S. Wrabetz, A. Mazheika, F. Girgsdies, D. Teschner, F. Seitz, A. Tarasov, S. V. Levchenko, R. Schlögl and E. Frei, *J. Am. Chem. Soc.*, 2019, **141**, 2451–2461.
11 L. Sandoval-Diaz, D. Cruz, M. Vuijk, G. Ducci, M. Hävecker, W. Jiang, M. Plodinec, A. Hammud, D. Ivanov, T. Götsch, K. Reuter, R. Schlögl, C. Scheurer, A. Knop-Gericke and T. Lunkenbein, *Nat. Catal.*, 2024, **7**, 161–171.
12 M. Akri, S. Zhao, X. Li, K. Zang, A. F. Lee, M. A. Isaacs, W. Xi, Y. Gangarajula, J. Luo, Y. Ren, Y. T. Cui, L. Li, Y. Su, X. Pan, W. Wen, Y. Pan, K. Wilson, L. Li, B. Qiao, H. Ishii, Y. F. Liao, A. Wang, X. Wang and T. Zhang, *Nat. Commun.*, 2019, **10**, 5181.
13 H. Wang, G. Cui, H. Lu, Z. Li, L. Wang, H. Meng, J. Li, H. Yan, Y. Yang and M. Wei, *Nat. Commun.*, 2024, **15**, 3765.
14 Q. Zhu, H. Zhou, L. Wang, L. Wang, C. Wang, H. Wang, W. Fang, M. He, Q. Wu and F.-S. Xiao, *Nat. Catal.*, 2022, **5**, 1030–1037.
15 Y. Tang, Y. Wei, Z. Wang, S. Zhang, Y. Li, L. Nguyen, Y. Li, Y. Zhou, W. Shen, F. F. Tao and P. Hu, *J. Am. Chem. Soc.*, 2019, **141**, 7283–7293.

16 C. Palmer, D. C. Upham, S. Smart, M. J. Gordon, H. Metiu and E. W. McFarland, *Nat. Catal.*, 2020, **3**, 83–89.
17 H. Lv, X. Dong, R. Li, C. Zeng, X. Zhang, Y. Song, H. Liu, J. Shao, N. Ta, Q. Zhao, Q. Fu, J. Xiao, G. Wang and X. Bao, *Nat. Chem.*, 2025, **17**, 695–702.
18 L. C. Buelens, V. V. Galvita, H. Poelman, C. Detavernier and G. B. Marin, *Science*, 2016, **354**, 449–452.
19 L. Zeng, Z. Cheng, J. A. Fan, L.-S. Fan and J. Gong, *Nat. Rev. Chem.*, 2018, **2**, 349–364.
20 X. Zhang, Y. Xu, Y. Liu, L. Niu, Y. Diao, Z. Gao, B. Chen, J. Xie, M. Bi, M. Wang, D. Xiao, D. Ma and C. Shi, *Chem*, 2023, **9**, 102–116.
21 S. Zhang, Z. Q. Huang, Y. Ma, W. Gao, J. Li, F. Cao, L. Li, C. R. Chang and Y. Qu, *Nat. Commun.*, 2017, **8**, 15266.
22 T. Montini, M. Melchionna, M. Monai and P. Fornasiero, *Chem. Rev.*, 2016, **116**, 5987–6041.
23 S. Zhang, Z. Tian, Y. Ma and Y. Qu, *ACS Catal.*, 2023, **13**, 4629–4645.
24 J. Graciani, K. Mudiyanselage, F. Xu, A. E. Baber, J. Evans, S. D. Senanayake, D. J. Stacchiola, P. Liu, J. Hrbek, J. F. Sanz and J. A. Rodriguez, *Science*, 2014, **345**, 546–550.
25 Z. Liang, T. Li, M. Kim, A. Asthagiri and J. F. Weaver, *Science*, 2017, **356**, 299–303.
26 Q. Cheng, X. Yao, L. Ou, Z. Hu, L. Zheng, G. Li, N. Morlanes, J. L. Cerrillo, P. Castano, X. Li, J. Gascon and Y. Han, *J. Am. Chem. Soc.*, 2023, **145**, 25109–25119.
27 Z. Rao, K. Wang, Y. Cao, Y. Feng, Z. Huang, Y. Chen, S. Wei, L. Liu, Z. Gong, Y. Cui, L. Li, X. Tu, D. Ma and Y. Zhou, *J. Am. Chem. Soc.*, 2023, **145**, 24625–24635.
28 M. Filez, V. De Coster, H. Poelman, V. Briois, A. Beauvois, J. Dendooven, M. B. J. Roeffaers, V. Galvita and C. Detavernier, *Nat. Catal.*, 2025, **8**, 187–195.
29 S. Kattel, P. Liu and J. G. Chen, *J. Am. Chem. Soc.*, 2017, **139**, 9739–9754.
30 S. Navarro-Jaén, M. Virginie, J. Bonin, M. Robert, R. Wojcieszak and A. Y. Khodakov, *Nat. Rev. Chem.*, 2021, **5**, 546–579.
31 R. Ye, J. Ding, T. R. Reina, M. S. Duyar, H. Li, W. Luo, R. Zhang, M. Fan, G. Feng, J. Sun and J. Liu, *Nat. Synth.*, 2025, **4**, 288–302.
32 S. Zhang, Y. Liu, M. Zhang, Y. Ma, J. Hu and Y. Qu, *Nat. Commun.*, 2022, **13**, 5527.
33 S. Zhang, Z. Xia, Y. Zou, F. Cao, Y. Liu, Y. Ma and Y. Qu, *J. Am. Chem. Soc.*, 2019, **141**, 11353–11357.
34 J. Ren, Y. Liu, Y. Wang, W. Guo, K. Ma, Y. Qu and S. Zhang, *ACS Nano*, 2026, **20**, 4470–4478.
35 E. Garand, T. Wende, D. J. Goebbert, R. Bergmann, G. Meijer, D. M. Neumark and K. R. Asmis, *J. Am. Chem. Soc.*, 2010, **132**, 849–856.
36 S. M. Jin, C. Kwon, A. Bugaev, B. Karakurt, Y. C. Lin, L. Savereide, L. P. Zhong, V. Boureau, O. Safonova, S. Kim and J. S. Luterbacher, *Nat. Catal.*, 2024, 1119–1212.
37 C. Vogt, E. Groeneveld, G. Kamsma, M. Nachtegaal, L. Lu, C. J. Kiely, P. H. Berben, F. Meirer and B. M. Weckhuysen, *Nat. Catal.*, 2018, **1**, 127–134.
38 W. Li, J. Gan, Y. Liu, Y. Zou, S. Zhang and Y. Qu, *Angew. Chem., Int. Ed.*, 2023, **62**, e202305661.
39 L. F. Bobadilla, J. L. Santos, S. Ivanova, J. A. Odriozola and A. Urakawa, *ACS Catal.*, 2018, **8**, 7455–7467.
40 H. Shen, Y. Dong, S. Yang, Y. He, Q. Wang, Y. Cao, W. Wang, T. Wang, Q. Zhang and H. Zhang, *Nano Res.*, 2022, **15**, 5831–5841.
41 W. Li, B. Liu, Q. Guo, W. Guo, S. Zhang and Y. Qu, *Nat. Commun.*, 2025, **16**, 7335.
42 F. Xue, C. Zhang, C. Cheng, X. Yan, F. Liu, X. Liu, B. Jiang, Q. Zhang, L. Sun, H. Peng, W. H. Huang, C. W. Pao, Z. Hu, M. Chen, D. Su, M. Liu, X. Huang and Y. Xu, *Nat. Commun.*, 2024, **15**, 10451.
43 J. Ma, C. Zhu, K. Mao, W. Jiang, J. Low, D. Duan, H. Ju, D. Liu, K. Wang, Y. Zang, S. Chen, H. Zhang, Z. Qi, R. Long, Z. Liu, L. Song and Y. Xiong, *Nat. Commun.*, 2023, **14**, 1410.
44 J. F. Weaver, C. Hakanoglu, A. Antony and A. Asthagiri, *Chem. Sev. Rev.*, 2014, **43**, 7536–7547.
45 Q. Fu, H. Saltsburg and M. Flytzani-Stephanopoulos, *Science*, 2003, **301**, 935–938.
46 K. Ding, A. Gulec, A. M. Johnson, N. M. Schweitzer, G. D. Stucky, L. D. Marks and P. C. Stair, *Science*, 2015, **350**, 189–192.